Engineering Science and Technology, an International Journal 47 (2023) 101549

Contents lists available at ScienceDirect

Engineering Science and Technology, an International Journal

journal homepage: www.elsevier.com/locate/jestch

Full Length Article

Independent-regulated double-edge Janus angular absorber for terahertz waves based on photonic edge band gaps and graphene wide-angle absorption

Bao-fei Wan, Hai-ning Ye, Hai-feng Zhang *

College of Electronic and Optical Engineering & College of Flexible Electronics (Future Technology), Nanjing University of Posts and Telecommunications, Nanjing 210023, China

ARTICLE INFO

Keywords:
Independent-regulated double edges
Janus angular absorber
Graphene material
Transmission angle window
Absorption angle window

ABSTRACT

In this paper, three categories of Janus angle absorption structures for terahertz (THz) waves are realized by operating the edge hopping property of the photonic band gaps (PBGs) and the wide-angle absorption of graphene heterostructure. The left and right edges of the angle window are determined by the PBGs generated by photonic crystals 1 (PC_1) and photonic crystals 2 (PC_2), respectively. The appropriate combination of the two can obtain a transmission angle window (TAW), and the edges can be independently manipulated, which makes it possible to construct arbitrary angle filtering structures, making up for the shortage of rigid angle windows in traditional research. Graphene material has absorption potential, and when it is introduced into ternary photonic crystals 3 (PC_3), high absorption at large angles will occur. The combination of PC_3 and TAW will produce an absorption angle window (AAW) by using the energy cascade transmission features of photonic crystals (PCs). Contributing to the strong absorption properties, the energy transfer on both sides of PC_3 is isolated. Consequently, the Janus angle absorption phenomenon will be remarkable by mirroring the PCs structures with different TAWs on both sides of PC_3. Through the unique parameter design, the three relationships between the forward AAW and the backward one are investigated, that is inclusion, partial coincidence, and incoherence.

1. Introduction

The terahertz (THz) band is located between the microwave and infrared bands, and the frequency range refers to 0.1 ~ 10 THz [1,2]. In recent years, with the development of THz source technology, the spectrum in this region has attracted a large number of researchers [3–5] in the fields of optical imaging, biological detection, optical communication, and perfect absorption, by its high security, strong penetrability, spectral resolution characteristics, and other advantages. For the sake of further filling the gap of THz, it is necessary to explore relevant devices and manipulation means from different levels, such as Janus transmission and polarization selection, which are critical technologies in optical communication. Janus is the Roman god of beginnings, who has two faces and looks into the past and the future [6]. Inspired by this, scientists named the two-sided particles Janus particles, which have different materials on opposite sides [7].

Recently, a similar Janus function has been extended to superstructures formed from artificially filled media. By destroying the symmetry of the structure, the regulation of different electromagnetic wave propagation directions is formed, which is the physical property and function that the natural structure does not have, and provides new freedom for the regulation of electromagnetic devices [8]. Janus optics selectively allow light to pass in one direction while absolutely shielding it in the opposite direction. Due to its unique optical charm, it has important application potential in compact optical components, from optical communication [9], isolators [10], sensing systems [11], signal processing [12], directed radiation [13], and other fields.

As a universal THz material, grapheme [14–16] is a two-dimensional honeycomb structure, whose thickness is equivalent to a single layer of carbon atoms. Benefiting from its unique optical, mechanical, and electronic properties, it has significant impacts on saturated absorption [17], optical detection [18], optical filtering [19], and other fields [20,21]. In the THz band, graphene material are provided with rich potential in improving the attenuation rate of radiation sources near its surface and designing Janus wide-angle absorbers, which have been greatly emphasized.

* Corresponding author.
E-mail address: hanlor@njupt.edu.cn (H.-f. Zhang).

https://doi.org/10.1016/j.jestch.2023.101549
Received 29 June 2023; Received in revised form 2 September 2023; Accepted 26 September 2023

In the process of optical development, the selectivity of frequency, angle, or polarization plays a fundamental and important role. The control of electromagnetic waves through these separate properties is of paramount significance to the research of electromagnetics. Relying on the massive exploration of predecessors, theoretical research and experimental verifications of frequency and polarization have been common, and the technologies are increasingly mature. Unfortunately, the regulation of propagation direction has perpetually been a scientific challenge, and the signs of progress remain relatively tardiness. Nevertheless, the operation of the angle domain has advantages that cannot be ignored for signal selection [22], energy acquisition [23], laser light source regulation [24], and image processing. Consequently, it is urgent to promote the exploration of related technologies.

Photonic crystals (PCs) [25–28] provide the possibility of manipulating dispersion patterns and have the potential for large-scale manufacturing. Fabry-Perot cavity [29,30] gets rid of polarization dependence, but due to its resonance particularities, it can only produce an angle selection at a single frequency point. The narrow band angle window can be generated based on Brewster angle mode [31,32], but this mode greatly depends on the TM polarization, not TE polarization. Theoretically, the polarization-independent angle selection structure is more representative in practical applications. The photonic band gaps (PBGs) [33,34] features are also possible for the generation of an angle window independent of the polarization, however, its angle selection stubbornly starts from 0 degrees and lacks tunability. In 2014, Shen *et al.* [35] proposed to use the Brewster angle principle of stack structure to design a transmission angle window (TAW) for the TM wave, where the medium permeability is not 1, increasing the difficulty of actual manufacturing. In 2016, Iizuka *et al.* [36] overcame the dilemma of polarization by using PBG and created a TAW with a starting angle of 0 degrees. Two years later [37], they verified it through experiments, and the simulation results were quite consistent with the measured data. In 2018 [38], Qu *et al.* improved the Brewster structure model by introducing a half-wave plate to achieve a polarization-independent TAW. Nevertheless, due to the existence of the stack structure, the resonance properties of the structure are difficult to offset, resulting in conspicuous room for improving the angle selectivity. In 2021 [39], Wan *et al.* presented the nonreciprocal polarization separation absorption angle window (AAW) based on the asymmetric arrangement. On the premise of maintaining high absorption and a strong rectangular coefficient, the quasi-periodic method is employed to broaden the frequency band, but its angle window still lacks tunability. Although predecessors have made indelible contributions to the investigations of angle technology, as far as we know, no systematic and marginal independent Janus angle structures have been reported.

In this paper, PBGs that generate energy transitions at different incident angles are constructed and spliced to form a TAW with independently controllable angle edges. Combined with the wide-angle absorption features of graphene heterostructure, and the TAWs with different angle ranges are mirrored on both sides of the absorption structure, the Janus AAW can be formed. Through ingenious parameter design, three states of the forward and backward incident windows appear, that is, inclusion relation, partial coincidence relation, and incoherence relation. We hope that the proposed design is meaningful for improving the investigation of THz technologies and angle selection structures.

2. Modeling and design

The proposed angle selection structure is described in Fig. 1. The left edge of the angle window is controlled by PCs 1 (PC_1), the right edge is operated by PCs 2 (PC_2), and the strong absorption is generated by PCs 3

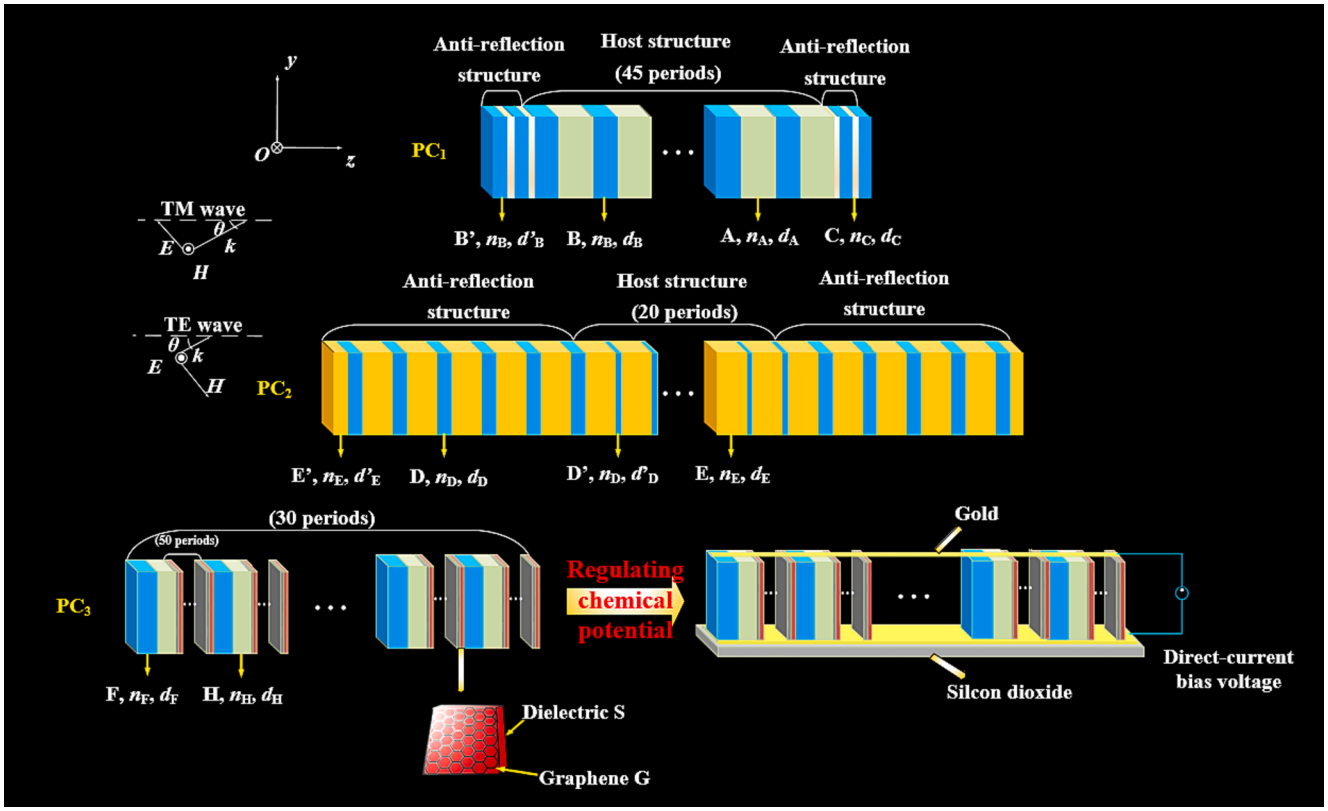

Fig. 1. The proposed angle selection structure diagram. The forward incident wave propagates in the direction of + *z* and the backward incident wave along the direction of -*z*. The angle between the wave vector *k* and the + *z* axis is the incident angle θ. The sequence of PC_1 is $(B'C)^2(BA)^{45}(CB')^2$. The sequence of PC_2 is $E'(DE)^5D(ED')^{20}(ED)^5E'$. The sequence of PC_3 is $(FH(GS)^{50})^{30}$. Where, dielectrics B, D and F have the same refractive index, and dielectrics A and H possess the same refractive index.

(PC_3). The combination of PC_1 and PC_2 induces the TAW, while the arrangement of PC_1, PC_2, and PC_3 excites the AAW. PC_1 consists of dielectrics A, B and C, and its sequence is $(B'C)^2(BA)^{45}(CB')^2$, where $(BA)^{45}$ is the host structure and the others are anti-reflection structures. Dielectric B and dielectric B' are the same material, but their thicknesses are different. PC_2 is composed of dielectrics D and E, and its arrangement belongs to $E'(DE)^5D(ED')^{20}(ED)^5E'$, in which, $(ED')^{20}$ is the host structure and the structures on both sides are anti-reflection structures. Similarly, D and D' are the same medium, so are E and E', but they have different thicknesses. The host structure is used to generate the angle selection phenomenon, while the anti-reflection structure is responsible for suppressing the reflection resonance in the angle window, which has been studied in detail in our previous work [39]. PC_3 is a ternary PCs structure made up of media F, H, G, and S and its distribution is $(FH(GS)^{50})^{30}$. μ indicates the externally controllable chemical potential of the graphene structure by modulating the external voltage. The feeding mode of a graphene structure is indicated in Fig. 1. The entire structure is placed on a silicon dioxide substrate, the gold electrodes at the top and bottom of the structure are in direct contact with the graphene structure, and a forward gate bias is applied to the gold electrode at the top. A negative voltage is connected to the gold electrode at the bottom. Therefore, applying direct-current bias voltage can effectively regulate the chemical potential [15].

Among them, the refractive indexes of the dielectrics A, B, C, D, E, F, H and S are $n_A = 3.3$, $n_B = 1.45$, $n_C = 2.15$, $n_D = 1.45$, $n_E = 2.3$, $n_F = 1.45$, $n_H = 3.3$, and $n_S = 3.33$ respectively, and the thicknesses are in turn $d_A = 42.24$ μm, $d_B = 30.65$ μm, $d_C = 1.8$ μm, $d'_B = 27.56$ μm, $d_D = 15.9$ μm, $d'_D = 15$ μm, $d_E = 36.5$ μm, $d'_E = 18.25$ μm, $d_F = 4$ μm, $d_H = 1$ μm, $d_S = 85$ nm. For the convenience of expression, only the refractive index of the medium is given here, which is a common expression in PCs research [35,38,39]. Of course, these media can be found in nature or synthesized artificially, but the design of materials is not the focus of this paper. Therefore, the specific details of materials are not studied in depth in this paper. G refers to the graphene material. The conductivity of the graphene can be calculated by the Kubo equation: [40]

$$\sigma_G = \sigma_G^{inter} + \sigma_G^{intra} \tag{1}$$

where σ_G^{inter} and σ_G^{intra} are the inter-band and intra-band conductivities of graphene, respectively [40].

$$\sigma_G^{intra} = \frac{ie^2 k_B T}{\pi\hbar^2(\omega + i/\tau)}\left(\frac{\mu}{k_B T} + 2\ln(e^{-\frac{\mu}{k_B T}} + 1)\right) \tag{2}$$

$$\sigma_G^{inter} = i\frac{e^2}{4\pi\hbar}\ln\left|\frac{2\mu - \hbar(\omega + i/\tau)}{2\mu + \hbar(\omega + i/\tau)}\right| \tag{3}$$

where e is the electron charge, kB is the Boltzmann constant, $T = 300$ K is the temperature, $\tau = 0.5$ ps is the relaxation time, and $\mu = 0.01$ ev is the chemical potential. If the electronic band structure of the graphene layer is not affected by external influences, then its dielectric function can be written as:

$$\varepsilon_G = 1 + i\sigma_G/\omega\varepsilon_0 d_G \tag{4}$$

Among them, $d_G = 0.34$ nm signifies the thickness of the graphene layer.

The connection between different media layers is achieved through the transfer matrix method as follows [28,41–44],

$$M = \begin{bmatrix} M_{11} & M_{12} \\ M_{21} & M_{22} \end{bmatrix} \tag{5}$$

The film matrix of each layer can be determined by the following forms,

$$M_i = \begin{bmatrix} \cos\delta_i & -jp_i^{-1}\sin\delta_i \\ -jp_i\sin\delta_i & \cos\delta_i \end{bmatrix} \tag{6}$$

Among them, $\delta_i = (2\pi/\lambda)n_i d_i \cos\theta_i$, where $\lambda = 2\pi c/\omega$, $c = 3 \times 10^8$ m/s, $p_i = \sqrt{\varepsilon_0/\mu_0}n_i\cos\theta_i$(TE wave), or $p_i = \sqrt{\varepsilon_0/\mu_0}n_i/\cos\theta_i$(TM wave). θ_i is the propagation angle of an electromagnetic wave in layer i. $\mu_0 = 4\pi \times 10^{-7}$H/m is the permeability of vacuum. $\varepsilon_0 = 8.854187817 \times 10^{-12}$F/m is the dielectric constant of the vacuum. $f = 3.26$ THz indicates the frequency. In the propagation direction, the magnetic field component fails to exist in the TM wave, and the electric field component is not owned by the TE wave.

The reflection coefficient r and transmission coefficient t can be described by the following formulas [40]:

$$r = \left|\frac{(M_{11} + M_{12}p_0)p_0 - (M_{21} + M_{22}p_0)}{(M_{11} + M_{12}p_0)p_0 + (M_{21} + M_{22}p_0)}\right| \tag{7}$$

$$t = \left|\frac{2p_0}{(M_{11} + M_{12}p_0)p_0 + (M_{21} + M_{22}p_0)}\right| \tag{8}$$

As a result, reflectivity R and transmittance T are presented as:

$$\begin{aligned} R &= |r|^2 \\ T &= |t|^2 \end{aligned} \tag{9}$$

The absorptivity A can be expressed as:

$$A = 1 - |r|^2 - |t|^2 \tag{10}$$

3. Results and discussion

In Fig. 2, the PBGs properties are excerpted to explain the angle selection phenomenon more evidently. First, the amplitude at 0 degrees

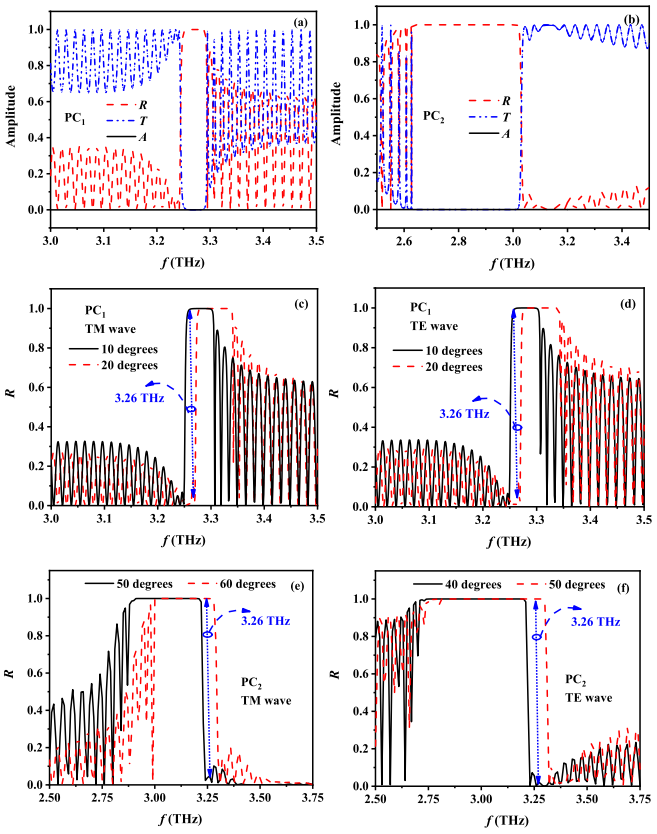

Fig. 2. The spectra of T, R, and A of a) PC_1, and b) PC_2 under the case of 0 degrees. The frequency domain energy jump of the left edge controlled by PC_1 near the critical angle c) of the TM wave incidence and d) of the TE wave incidence. The frequency domain energy jump of the left edge controlled by PC_2 near the critical angle e) of the TM wave incidence and f) of the TE wave incidence.

incidence is analyzed. Since the TE and TM waves exhibit the same electromagnetic response characteristics at 0 degrees, only the TM wave is shown in Fig. 2**a and b**. In Fig. 2**a**, for PC_1, PBG occurs in the frequency range 3.248 ~ 3.292 THz. Within PBG, the reflectivity is higher than 0.9, the transmittance is lower than 0.1, and the absorptivity tends to 0. In Fig. 2**b**, for PC_2, PBG appears in the range of 2.585 ~ 3.025 THz. Similarly, the phenomena of high reflection and low transmission are satisfied in PBG, while the absorption is also close to 0. With the increase of angle, PBG will generate a frequency shift, and the rectangular character of PBG will also be maintained during the movement, which is conducive to the formation of the TAW. In Fig. 2**c**, in the case of the TM wave incidence, for the left edge of the angle window controlled by PC_1, during the transition of the incidence angle from 10 degrees to 20 degrees, the left edge of the PBG is blue-shifted, and the state at 3.26 THz jumps from total reflection to transmission. In Fig. 2**d**, for the TE wave, the left edge generated by PC_1 will have a similar phenomenon. In Fig. 2**e**, the right edge of the angle window determined by PC_2 will also blue shift during the transition of the incident angle from 50 degrees to 60 degrees, and the electromagnetic wave energy is faced with the transition from high transmission to strong reflection at 3.26 THz. In Fig. 2**f**, if the polarization wave changes from the TM wave to the TE wave, the hurricane of amplitude state will occur in the region of 40 ~ 50 degrees.

To more clearly demonstrate the propagation of electromagnetic wave energy near the PBG edges, the electric field energy distribution circumstances of $f = 3.26$ THz are provided. In Fig. 3**a**, for the TE wave edge, when θ is 10 degrees, the electric field is only displayed near the incident port, suggesting that the electromagnetic wave resonates with the structure only near the port, and then is completely reflected and fails to pass through the structure. However, at the incidence of 20 degrees, the entire structure presents extremely high electric field energy distribution, which means that electromagnetic waves can pass through the structure smoothly. In Fig. 3**b**, for the TM wave, if the incident angle is 10 degrees, the electric field energy only exists near the port and is not fully reflected through the structure. When the incident angle is 20 degrees, the whole structure is full of energy, which represents the smooth passage of electromagnetic energy, resulting in a transmission phenomenon. Through the analysis of the left edge, it is not difficult to find that the energy distribution of the two edge states is consistent with the frequency domain shown in Fig. 3**a and b**. In Fig. 3**c and d**, as to the right edge, the electric field energy distribution is similar to that of the left one, so details will not be elaborated.

In Fig. 4**a**, under the case of the TM wave, when PC_1 acts alone, the energy is completely reflected in the range of incidence angle less than 10 degrees. In the range of 10 ~ 20 degrees, the energy has a transition from strong reflection to high transmission. The selectivity near the critical angle is significant, and the transmissivity is higher than 0.85. If only PC_2 is working, the energy starts to reveal a transmission state from 0 degrees to a total reflection phenomenon in the area of 50 ~ 60 degrees. While maintaining a good angle selectivity, the transmissivity near the critical angle is also higher than 0.85. Naturally, it is assumed that the combination of PC_1 and PC_2 will create a TAW with double edges by virtue of the energy transfer characteristics of the PCs. As exhibited by the green ball in the figure, the composite structure forms an angle window with transmissivity higher than 0.85 in the range of 15.7 ~ 54.4 degrees, and the left and right edges are independently controlled by PC_1 and PC_2 respectively. Similarly, in Fig. 4**b**, when the TE wave is incident, PC_1 produces reflection → transmission state change in the range of 10 ~ 20 degrees, while PC_2 promotes the transition of transmission → reflection phenomenon in the range of 40 ~ 50

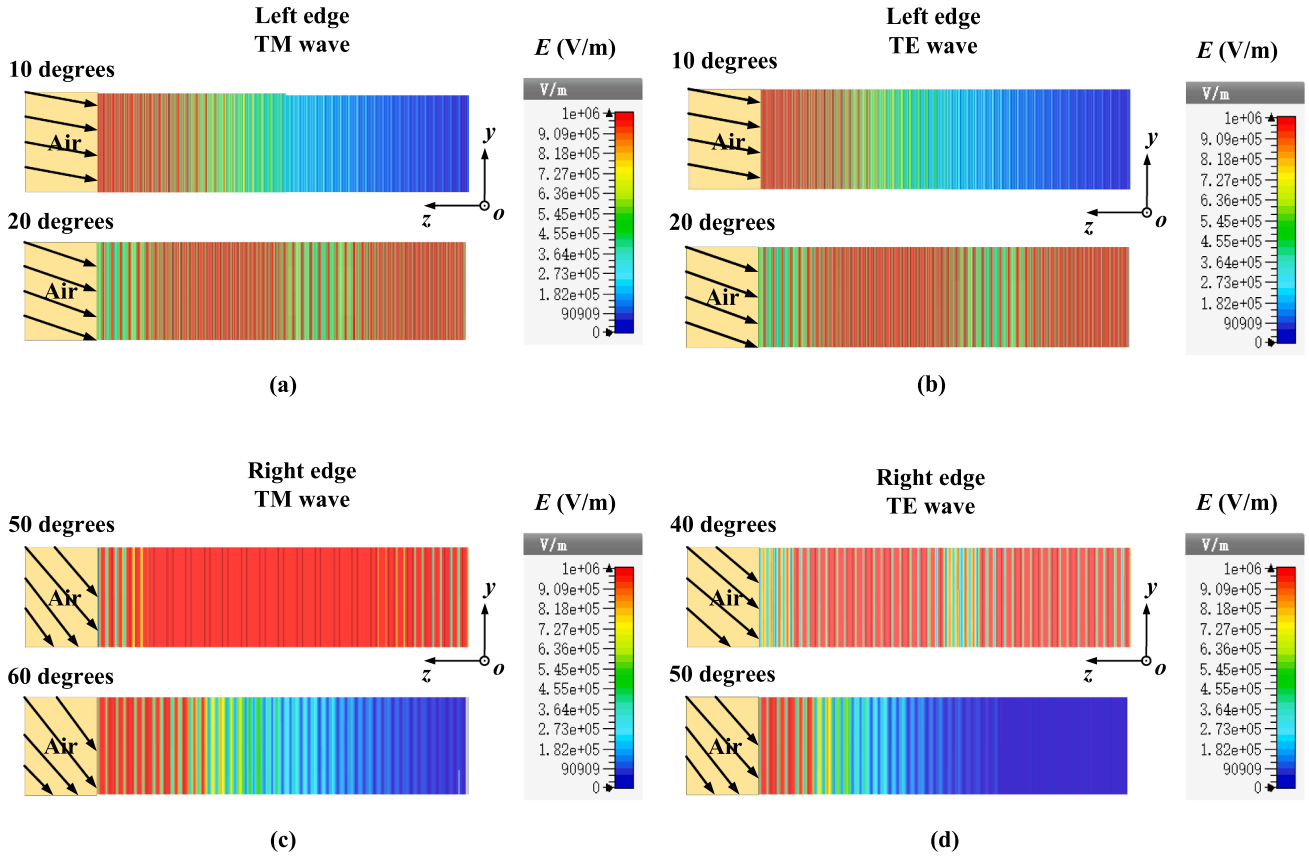

Fig. 3. $f = 3.26$ THz, for the left edge, a) the energy states of the TM wave at different incident angles, and b) the energy states of the TE wave at different incident angles. For the right edge, c) the energy states of the TM wave at different incident angles, and d) the energy states of the TE wave at different incident angles. The black arrow indicates the angle of the electromagnetic wave from the air to the host structure.

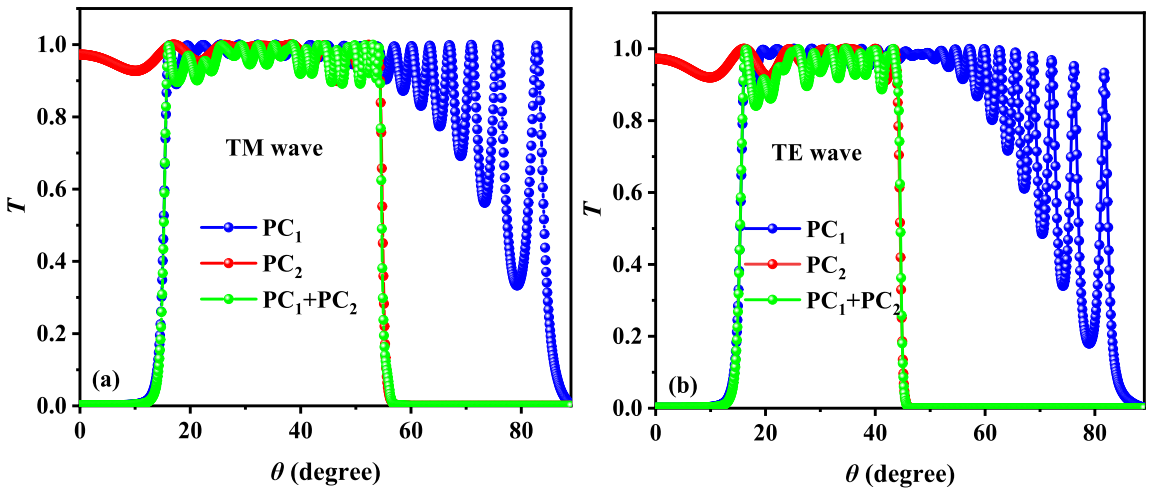

Fig. 4. The angle selection under the sole action of PC_1 or PC_2 and the TAW after the combination of both a) under the TM wave and b) under the TE wave.

degrees, and the transmission amplitudes at the critical angle exceed 0.85. The TAW with 15.9 ~ 44.2 degrees appears after the combination of two PCs. The double edges still maintain productive selectivity and the entire window shows fruitful filtering performance. At the same time, significant polarization separation occurs between the two polarization waves at large angles, with separation angles of 44.2 ~ 54.4 degrees.

As analyzed in Fig. 4, the left and right edges of the TAW are controlled by PC_1 and PC_2 respectively, meaning that the two sides can be adjusted independently, which is critical for the angle filters. In Fig. 5**a**, if the refractive index of the position where dielectric B is located is adjusted, and n_B rises from 1.42 to 1.48, the left edge moves from 11.5 degrees to 19.5 degrees, while the right edge fails to produce any offset. When the TM wave is still the incident wave, in Fig. 5**b**, if n_D is modulated and the refractive index is manipulated to the same range, only the right edge tends to increase from 51.3 degrees to 57.6 degrees. For the TE wave, similar manipulation results are also apparent. In Fig. 5**c**, provided that n_B changes, the range of the left edge is 11.6 ~ 19.8 degrees, while in Fig. 5**d**, n_D operates the right edge from 41.8 degrees to 46.8 degrees. Remarkably, no matter what the polarization wave is, the control of the edge of the TAW is independent of each other. This phenomenon benefits from the tunable properties of PBG. The adjustment of the refractive index of the dielectric obviously alters the position of PBG, thus affecting the critical jump position in the angle

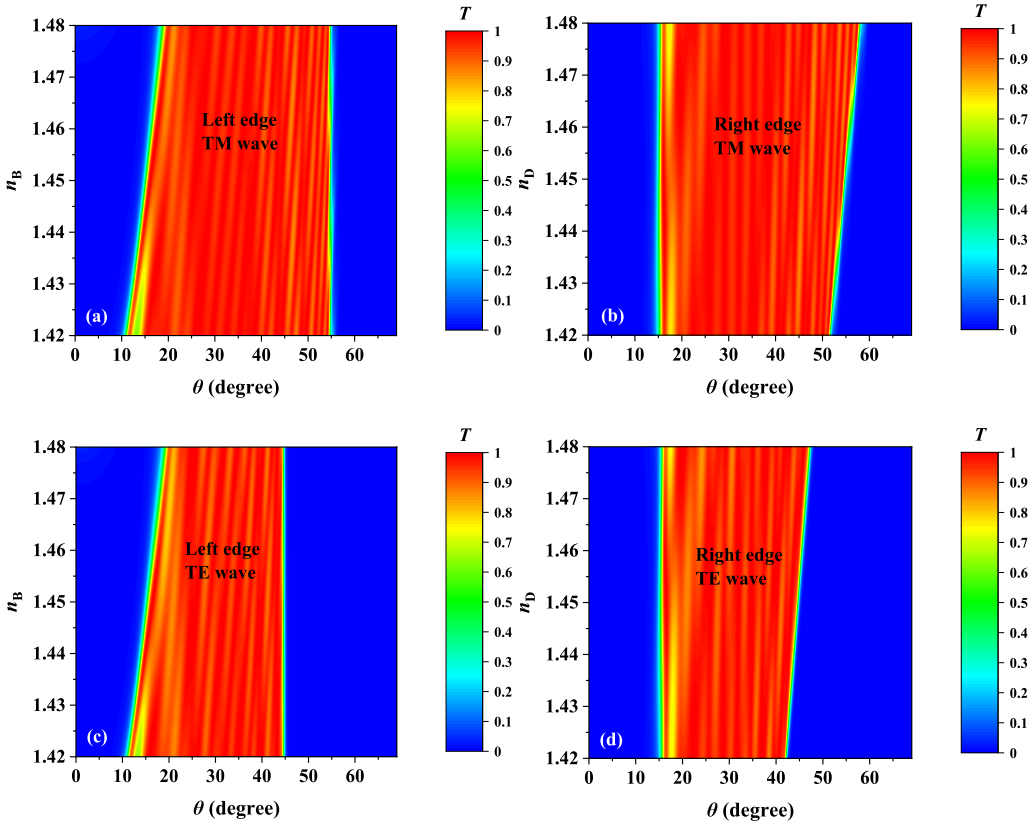

Fig. 5. In the case of the TM wave incidence, a) the regulation of n_B on the left edge, and b) the regulation of n_D on the right edge. In the case of the TE wave incidence, c) the regulation of n_B on the left edge, and d) the regulation of n_D on the right edge.

domain, resulting in the movement of the TAW.

In Fig. 6, the absorption properties of graphene structures are discussed. In Fig. 6**a**, for the TM wave, the absorption efficiency is very low when the unit structure consists of only a single layer of graphene G and a single layer of dielectric S. But if the number of periods is increased to 50, then the absorption rate can be increased to 0.3. If the $(GS)^{50}$ is periodically arranged with other media, the absorption will be further improved to more than 0.9. In Fig. 6**b**, for the frequency of 3.26 THz, there is also a wide-angle absorption characteristic, achieving an absorption higher than 0.9 in the range of 0 ~ 70 degrees. In Fig. 6**c and d, a** similar phenomenon occurs for the TE wave.

In Fig. 7**a and b**, no matter whether for the TM wave or the TE wave, the absorption intensity presents a law of first increasing and then decreasing with the rise of τ, and the absorptivity is the highest when τ = 0.5 ps. In Fig. 7**c and d**, for both polarized waves, the absorption intensity gradually attenuates with the augmentation of μ, and the higher the value of μ, the faster the absorptivity falls down.

According to Fig. 5, the combination of PC_1 and PC_2 shapes a TAW with double edges. If PC_3 is added, an AAW will be formed, and due to the strong absorption of PC_3, the energy on both sides is difficult to interfere with. Provided that the original PC_1 and PC_2 are placed on the other side of PC_3 in a mirror arrangement, and different angle windows are set, the Janus angle selection phenomenon will appear, which has been reported in our previous work [39]. The corresponding adjustment is not complicated, because the double edges of the angle window are moved independently, and only some thickness parameters in the PC_1 or PC_2 need to be fine-adjusted. Based on this design principle, three different Janus forms are explored.

In Fig. 8, for the PC_1 and PC_2 on the left side of the PC_3, $d_A = 42.24$ μm, $d_B = 30.65$ μm, $d_C = 1.8$ μm, $d'_B = 27.56$ μm, $d_D = 15.9$ μm, $d'_D = 15$ μm, $d_E = 36.5$ μm, $d'_E = 18.25$ μm. However, for PC_1 and PC_2 arranged on the right side of PC_3 in mirror mode, $d_A = 42.5$ μm, $d_B = 31$ μm, $d_C = 1.8$ μm, $d'_B = 28$ μm, $d_D = 15.9$ μm, $d'_D = 15$ μm, $d_E = 35.5$ μm, $d'_E = 17.75$ μm. The other parameters are the same as the above, and only the thicknesses of the media involved in PC_1 and PC_2 are adjusted. In Fig. 8**a**, if the TM wave is incident from the front, the AAW range is 15.7 ~ 54.3 degrees, while from the back, the angle range is 24 ~ 42.7 degrees, and the forward area completely covers the backward area. In Fig. 8**b**, for the TE wave incidence, the forward AAW range is 15.9 ~ 44.3 degrees, and the reverse range is 24.5 ~ 35.3 degrees. Similarly, the backward area is completely included in the forward range. Remarkably, by adjusting the medium thickness of the PCs on both sides of the PC_3, the dissimilation angle window is designed to achieve the Janus angle absorption phenomenon, which is also polarization-independent.

Inspired by Fig. 5, there also exists edge-independent regulation in the AAW. In Fig. 9**a and b**, for the forward incidence, the left and right edges of the TM wave are respectively controlled by n_B and n_D, and there is no interference between the edges, which has the potential of independent regulation of the angle window. In Fig. 9**c and d**, the double edges of the TE wave are also regulated by n_B and n_D. For the backward incidence, similar regulatory properties also arise in Fig. 9**(e)-(h)**. It is worth noting that in Fig. 9**e** and **g**, a refractive index higher than 1.46 will cause electromagnetic leakage in the case of weak incidence. For the angular absorption structure, we hope to achieve high absorption characteristics within the designed angle window, while outside the angle window, the electromagnetic wave is completely reflected.

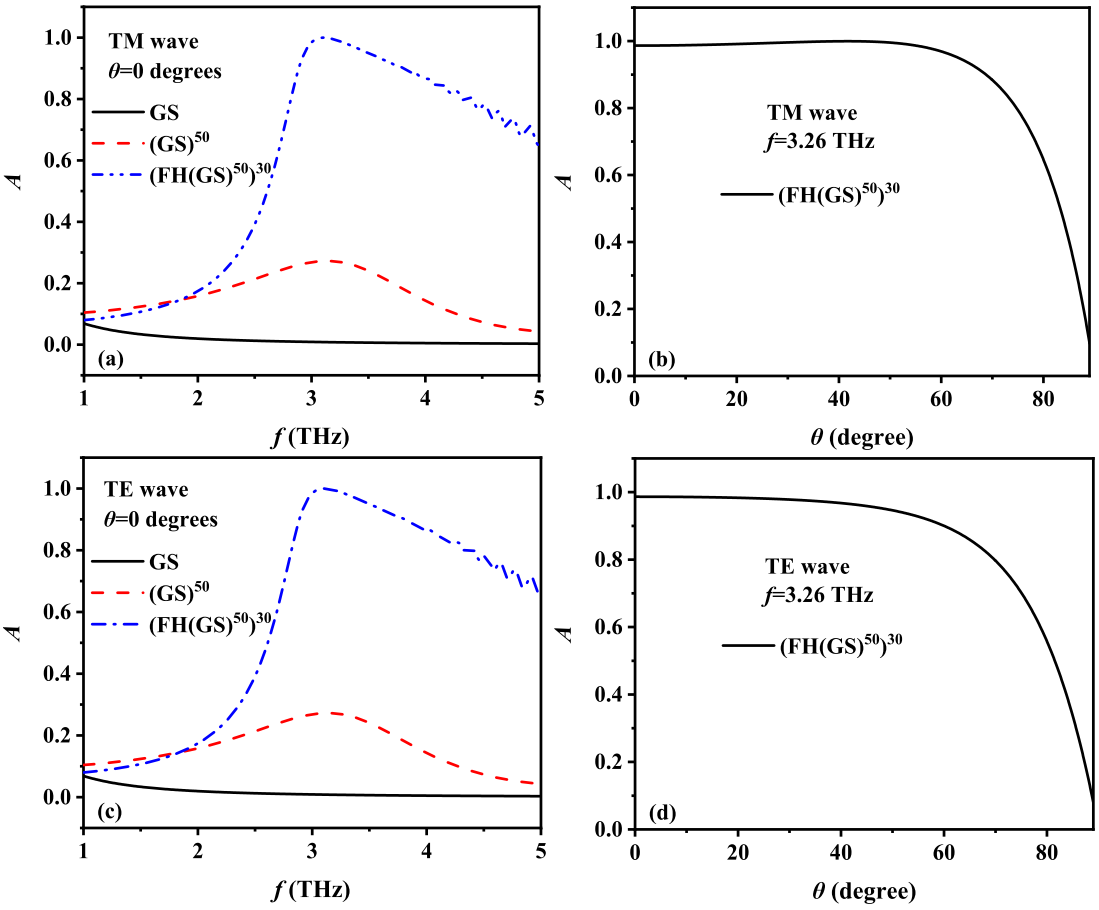

Fig. 6. Under the TM wave, a) the absorption properties of different graphene structures in the frequency domain, b) the absorption properties of $(FH(GS)^{50})^{30}$ structure in the angle domain. Under the TE wave, c) the absorption properties of different graphene structures in the frequency domain, d) the absorption properties of $(FH(GS)^{50})^{30}$ structure in the angle domain.

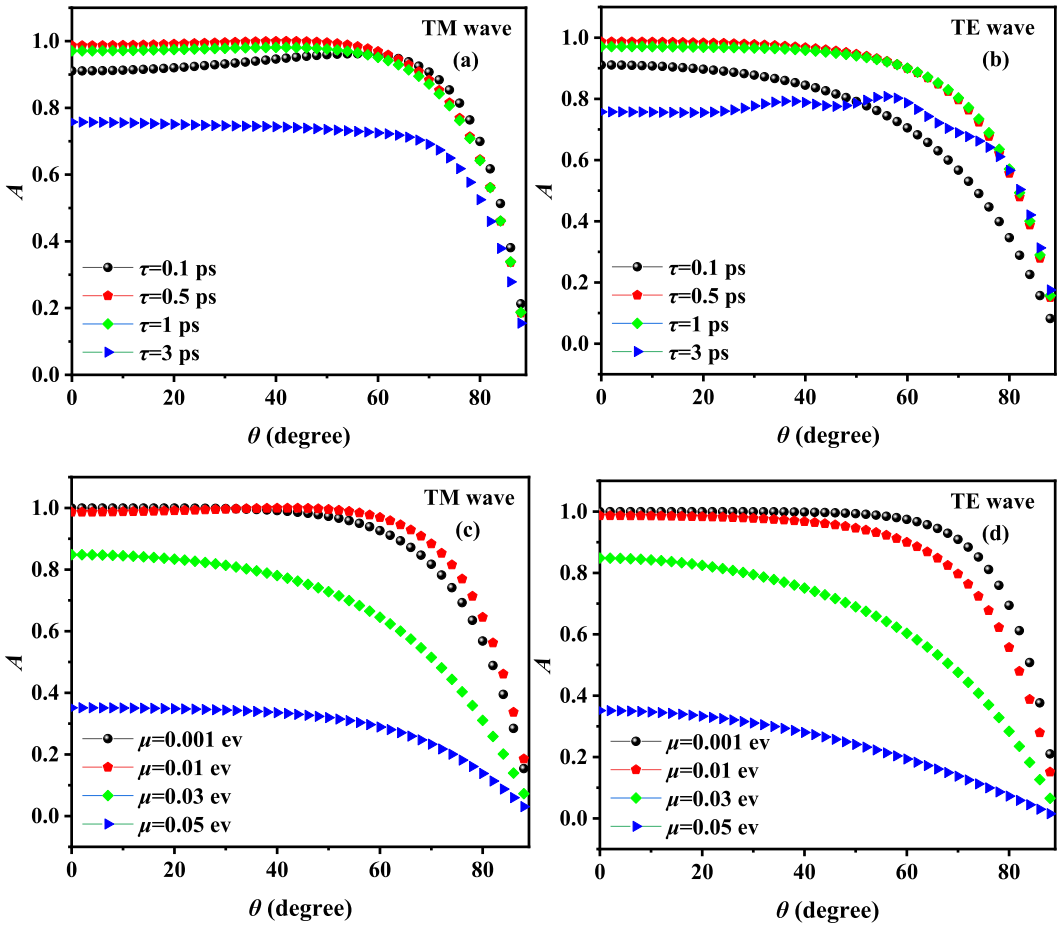

Fig. 7. The effects of relaxation time on absorption under a) the TM wave, and b) the TE wave. The effects of chemical potential on absorption under c) the TM wave, and d) the TE wave.

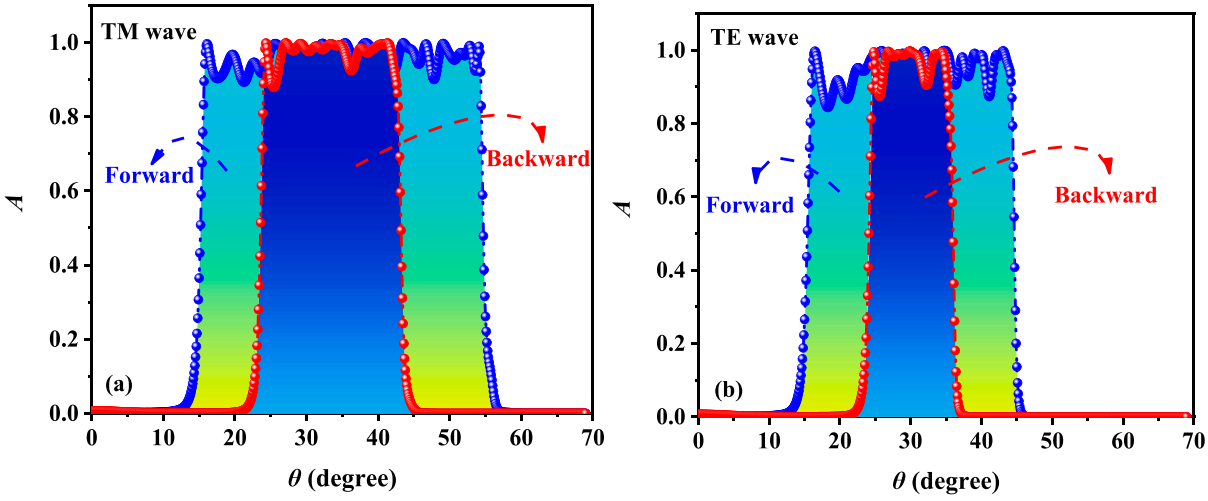

Fig. 8. Inclusive Janus absorption features corresponding to forward propagation and backward propagation under the case of a) the TM wave and b) the TE wave.

However, it is unrealistic to rely solely on the host structure in the model figure, and additional anti-reflection structures are needed to achieve impedance matching. Within the angle window, impedance matching is good, so the electromagnetic wave is completely absorbed, while outside the angle window, impedance matching is completely mismatched, so the electromagnetic wave is completely reflected. However, the range of such impedance matching is limited. Therefore, when the refractive index of the medium changes, the anti-reflection structure cannot be completely mismatched with the host structure in some angle regions, so the phenomenon of electromagnetic wave leakage appears. In general, n_B serves as a regulator of the left edge. Its enhancement drives the left edge to move towards a large angle, while the right edge is unaffected, forcing the AAW to gradually shrink. Unlike the former, n_D causes the right edge to drift toward a large angle, while the left edge is out of the

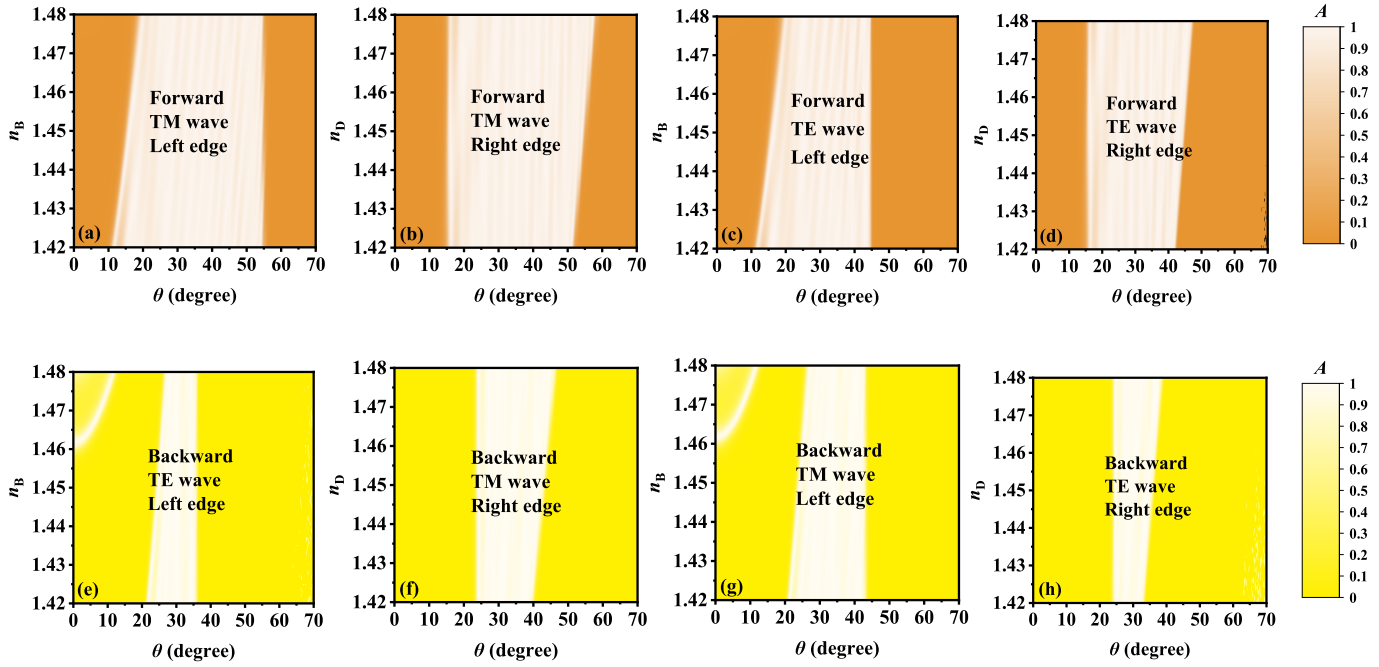

Fig. 9. A)-d) in the case of forward incidence, the changes ofn_B and n_D independently regulate the edges of the two polarized waves. e)-h) In the case of backward incidence, the adjustments of n_B and n_D independently regulate the edges of the two polarized waves.

way, driving the AAW to expand significantly. Similarly, for the four corresponding cases of forward and backward incidence, the relationship of angle inclusion exists all the time. The specific phenomena can be observed in Fig. 9**a and e**, Fig. 9**b and f**, Fig. 9**c** and **g**, and Fig. 9**d** and **g**.

In Fig. 10, for PC_1 and PC_2 on the left side of the PC_3, $d_A = 42.24$ μm, $d_B = 30.65$ μm, $d_C = 1.8$ μm, $d'_B = 27.56$ μm, $d_D = 15.9$ μm, $d'_D = 15$ μm, $d_E = 35.5$ μm, $d'_E = 17.75$ μm. Nevertheless, for PC_1 and PC_2 arranged on the right side of PC_3 in mirror mode, $d_A = 42.4$ μm, $d_B = 31.1$ μm, $d_C = 1.1$ μm, $d'_B = 28$ μm, $d_D = 15.8$ μm, $d'_D = 14.9$ μm, $d_E = 36.5$ μm, $d'_E = 18.25$ μm. In Fig. 10**a**, if the TM wave is in forward incidence, the range of AAW is 16 ~ 42.7 degrees, while from the back, the angle range is 22.4 ~ 53.6 degrees, and the forward and the backward areas partially coincide in the range of 22.4 ~ 42.7 degrees. In Fig. 10**b**, for the TE wave incidence, the forward angle absorption range is 16.1 ~ 35.6 degrees, and the reverse range is 22.8 ~ 44 degrees. Similarly, the angles in the opposite direction have overlapping parts between 22.8 degrees and 35.6 degrees. In Fig. 11**a, c, e**, and **g**, no matter whether the forward wave or the backward wave is working, the rise of n_B independently pushes the left edge to move to a large angle, thus tightening the AAW, and this movement trend does not depend on polarization. In Fig. 11**b, d, f**, and **h**, in the cases of the TM and TE waves incidence, the accession of n_D expands the selectivity of the right edge and further extends the AAW. By observing the combination of Fig. 11**a and e**, Fig. 11**b and f**, Fig. 11**c** and **g**, and Fig. 11**d** and **h**, it is not difficult to find that in the process of edge regulation, the relationship of partial coincidence of angle windows is always sustained. Attentionally, in Fig. 11**e** and **g**, when the left edge of the backward incident wave is controlled, the refractive index is not suitable for continuous expansion, and when it is higher than 1.46, energy leakage in a small angle range is induced.

In Fig. 12, for PC_1 and PC_2 on the left side of the PC_3, $d_A = 42.24$ μm, $d_B = 30.65$ μm, $d_C = 1.8$ μm, $d'_B = 27.56$ μm, $d_D = 15.7$ μm, $d'_D = 15$ μm, $d_E = 34.4$ μm, $d'_E = 17.2$ μm. However, for the PC_1 and PC_2 arranged on the right side of PC_3 in mirror mode, $d_A = 43.2$ μm, $d_B = 30.2$ μm, $d_C = 1.8$ μm, $d'_B = 30$ μm, $d_D = 15.9$ μm, $d'_D = 15$ μm, $d_E = 36.5$ μm, $d'_E = 18.25$ μm. In Fig. 12**a**, if the TM wave is incident frontally, the AAW is 15.8 ~ 28.4 degrees. Inversely, the angle range is 34.7 ~ 54.1 degrees,

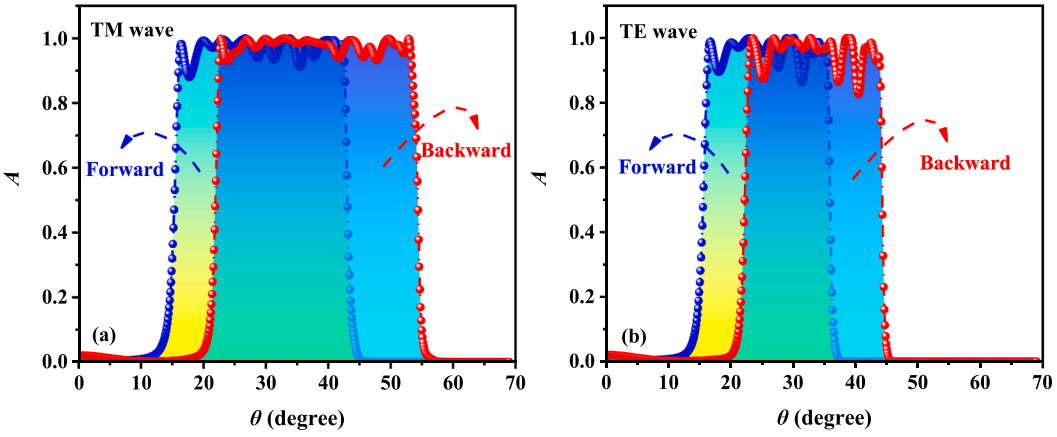

Fig. 10. The forward absorption and backward absorption correspond to the Janus absorption characteristics of the partially coincident type under the case of a) the TM wave and b) the TE wave.

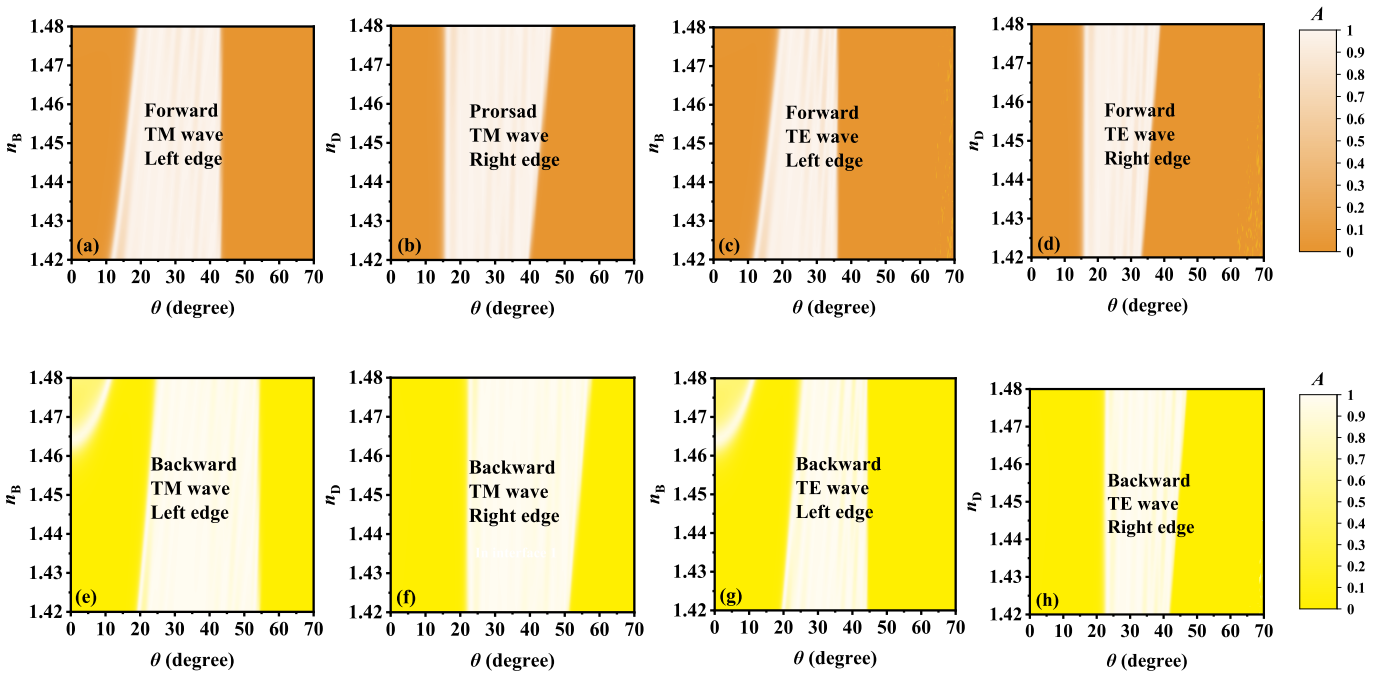

Fig. 11. A)-d) in the case of forward incidence, the changes ofn_B and n_D independently regulate the edges of the two polarized waves. e)-h) In the case of backward incidence, the adjustments of n_B and n_D independently regulate the edges of the two polarized waves.

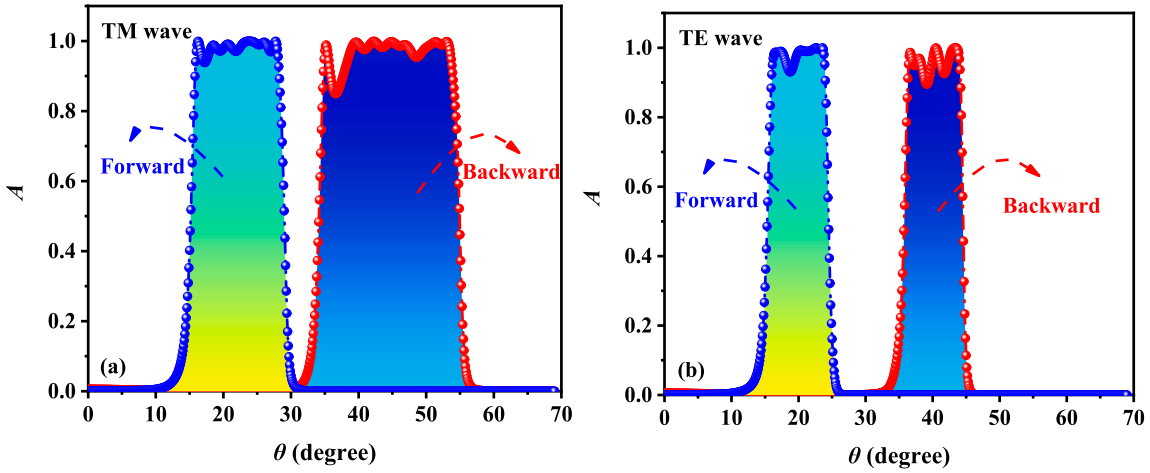

Fig. 12. Incoherent Janus absorption idiosyncrasies corresponding to the forward propagation and backward propagation under the case of a) the TM wave, and b) the TE wave.

and the forward area is completely separated from the backward area. In Fig. 12**b**, for the TE wave incidence, the forward AAW is 15.9 ~ 24 degrees, and the reverse range is 36.2 ~ 44.2 degrees. In addition, the range of angles in the opposite direction is completely separated. Similarly, incoherent Janus AAW also possesses the features of edge-independent operation. In Fig. 13**a and c**, n_B accurately controls the range of the left edge of different polarization waves under the action of the forward wave, while the right edge is stable. On the contrary, n_D is equipped with the ability to independently drive the active trajectory of the right edge in Fig. 13**b and d**. For the backward incidence, n_B in Fig. 13**e** and **g** and n_D in Fig. 13**f** and **h** play the same role as the former. The rise of n_B causes the angle window to shrink while the rise of n_D expands the angle window. By comparing Fig. 13**a and e**, Fig. 13**b and f**, Fig. 13**c** and **g**, and Fig. 13**d** and **h**, the incoherent angle window is always clear during the adjustment process, which can be explored. Additionally, in Fig. 13**a and c**, if the left edge of the forward wave is operated, the refractive index is not appropriate for continuous expansion, and a refractive index higher than 1.46 will cause electromagnetic leakage in the case of weak incidence.

Many angle absorption structures have been designed by using photonic crystal structures [45–53]. In order to show the advantages of this design, some representative works are selected and compared. In Table 1, the angle selectivity, tunability, and three types of Janus absorption are compared respectively. Among them, the degree of angle selectivity can be characterized by a rectangular coefficient. The formula for calculating the rectangle coefficient can be defined as the ratio of the angle window width of −3 dB to the angle window width of −30 dB [39]. The rectangle coefficient ranges from 0 to 1, and the higher the value, the stronger the angle selectivity. For comparison purposes, we consider a value above 0.8 to be highly selective, a value below 0.8 to be low selective, and a value tending to 0 to be non-selective. By comparison, it is not difficult to find that, according to the reported references,

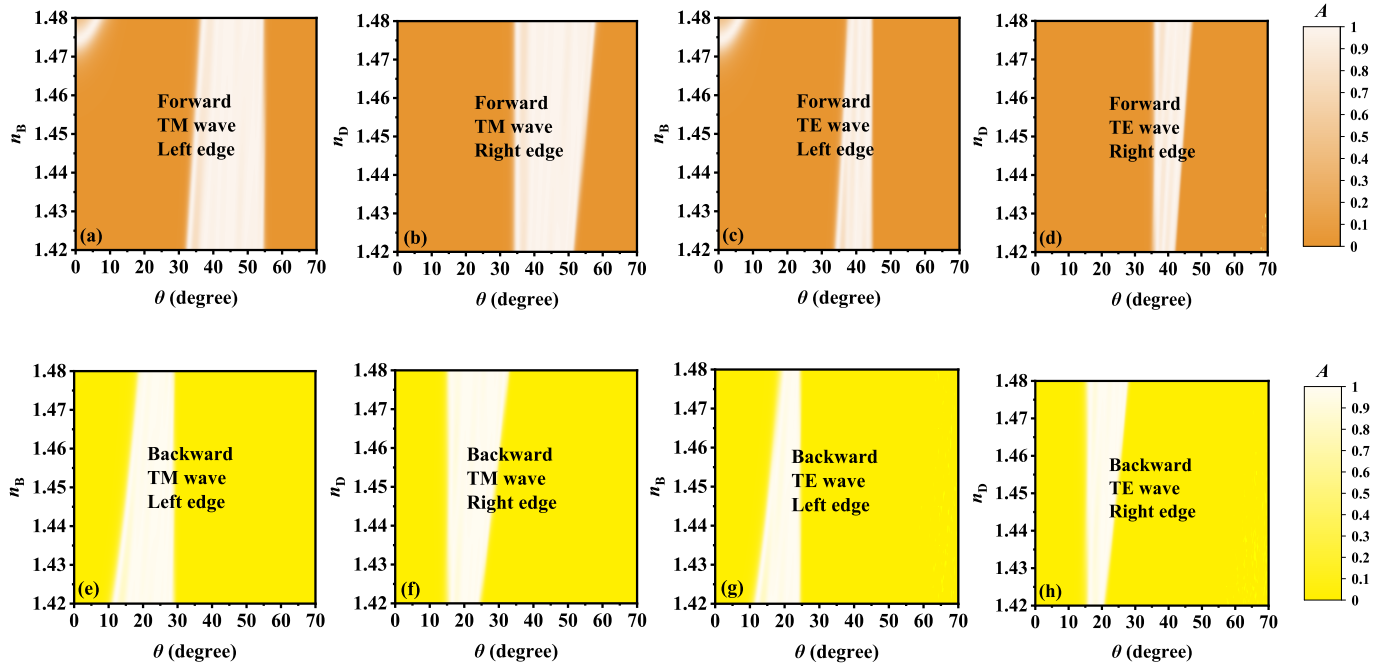

Fig. 13. A)-d) in the case of forward incidence, the changes ofn_B and n_D independently regulate the edges of the two polarized waves. e)-h) In the case of backward incidence, the adjustments of n_B and n_D independently regulate the edges of the two polarized waves.

Table 1
Comparison with previous works.

Ref.	Year	Absorber	Angle selectivity	Tunability	Janus		
					Inclusion	Partial coincidence	Incoherence
47	2016	Yes	Low	None	None	None	None
48	2017	Yes	Low	None	None	None	None
49	2018	Yes	None	None	None	None	Yes
50	2020	Yes	Low	None	None	None	None
39	2021	Yes	High	Yes	Yes	None	None
13	2021	Yes	High	Yes	None	None	None
51	2021	Yes	None	None	Yes	None	None
52	2021	Yes	Low	None	None	None	None
This work	2023	Yes	High	Yes	Yes	Yes	Yes

our structure fully achieves high selectivity, significant tunability, and three types of Janus absorption.

4. Conclusion

In this paper, the PBGs edge features of PCs, the wide-angle absorption of graphene heterostructure, and the asymmetric topological arrangement technology are jointly adopted to realize three different Janus AAWs, that is, inclusion relation, partial coincidence relation, and incoherence relation. The two edges of the AAWs are controlled by different PCs, so they can be independently manipulated by the refractive indexes of different media. In the process of regulation, the three Janus relationships can always be maintained. In addition, whether the TM wave or the TE wave is incident, the above performances are all satisfied, and a certain polarization separation phenomenon occurs in the case of a large angle. We hope that the proposed technology will be helpful to the development of angular selectivity and Janus technologies in the THz band. Of course, the biggest regret of this paper is that the results are purely based on theoretical simulation, and the experimental conditions in our university are not enough to support experimental verification. We strongly believe that our findings can be proven by other qualified teams in the future. We are also actively looking for cooperative teams and research funds to complete our follow-up work. We hope to complete the corresponding experimental verification work as soon as possible.

Declaration of Competing Interest

The authors declare that they have no known competing financial interests or personal relationships that could have appeared to influence the work reported in this paper.

Acknowledgment

This work is supported by the Postgraduate Research & Practice Innovation Program of Jiangsu Province (Grant No. KYCX23_1004).

References

[1] M. Tonouchi, Cutting-edge terahertz technology, Nature Photon. 1 (2) (2007) 97–105.
[2] N.T. Yardimci, S.-H. Yang, C.W. Berry, M. Jarrahi, High-power terahertz generation using large-area plasmonic photoconductive emitters, IEEE Trans. Terahertz Sci. Technol. 5 (2) (2015) 223–229.
[3] X. Cai, A.B. Sushkov, R.J. Suess, M.M. Jadidi, G.S. Jenkins, L.O. Nyakiti, R. L. Myers-Ward, S. Li, J. Yan, D.K. Gaskill, T.E. Murphy, H.D. Drew, M.S. Fuhrer, Sensitive room-temperature terahertz detection via the photothermoelectric effect in graphene, Nat. Nanotechnol. 9 (10) (2014) 814–819.

[4] Q. Wang, X. Zhang, E. Plum, Q. Xu, M. Wei, Y. Xu, H. Zhang, Y.i. Liao, J. Gu, J. Han, W. Zhang, Polarization and frequency multiplexed terahertz meta-holography, Adv. Opt. Mater. 5 (14) (2017).
[5] Y. Wu, C. La-o-vorakiat, X. Qiu, J. Liu, P. Deorani, K. Banerjee, J. Son, Y. Chen, E.E. M. Chia, H. Yang, Graphene terahertz modulators by ionic liquid gating, Adv. Mater. 27 (11) (2015) 1874–1879.
[6] Y. Zhu, L. Cao, A. Merkel, S. Fan, B. Vincent, B. Assouar, Janus acoustic metascreen with nonreciprocal and reconfigurable phase modulations, Nat. Commun. 12 (2021) 7089.
[7] Y.B. Zhang, et al., Direct observation of a widely tunable bandgap in bilayer grapheme, Nature 459 (2009) 820–823.
[8] A.-Y. Lu, H. Zhu, J. Xiao, C.-P. Chuu, Y. Han, M.-H. Chiu, C.-C. Cheng, C.-W. Yang, K.-H. Wei, Y. Yang, Y. Wang, D. Sokaras, D. Nordlund, P. Yang, D.A. Muller, M.-Y. Chou, X. Zhang, L.-J. Li, Janus monolayers of transition metal dichalcogenides, Nat. Nanotechnol. 12 (8) (2017) 744–749.
[9] L.i. Fan, J. Wang, L.T. Varghese, H. Shen, B. Niu, Y.i. Xuan, A.M. Weiner, M. Qi, An All-Silicon Passive Optical Diode, Science 335 (6067) (2012) 447–450.
[10] D. Jalas, A. Petrov, M. Eich, W. Freude, S. Fan, Z. Yu, R. Baets, M. Popović, A. Melloni, J.D. Joannopoulos, M. Vanwolleghem, C.R. Doerr, H. Renner, What is - and what is not - an optical isolator, Nat. Photonics 7 (8) (2013) 579–582.
[11] G. Dong, R. Liu, B.o. Lv, T. Lv, Y. Li, P. Li, Z. Zhu, C. Guan, J. Shi, Background-free metamaterial sensor based on resonant asymmetric transmission, Photon. Nanostruct. 40 (2020) 100792.
[12] D. Frese, Q. Wei, Y. Wang, L. Huang, T. Zentgraf, Nonreciprocal asymmetric polarization encryption by layered plasmonic metasurfaces, Nano Lett. 19 (6) (2019) 3976–3980.
[13] J. Xu, J. Mandal, A.P. Raman, Broadband directional control of thermal emission, Science 372 (6540) (2021) 393–397.
[14] Y.O. Averkov, V.M. Yakovenko, V.A. Yampol'skii, F. Nori, Terahertz transverse-electric- and transverse-magnetic-polarized waves localized on graphene in photonic crystals, Phys. Rev. B 90 (4) (2014), 045415.
[15] L. Qi, C. Liu, S.M. Ali Shah, A broad dual-band switchable graphene-based terahertz metamaterial absorber, Carbon 153 (2019) 179–188.
[16] H.J. Li, Y. Zhang, H.X. Xiao, M. Qin, S.X. Xia, L.L. Wang, Investigation of acoustic plasmons in vertically stacked metal/dielectric/graphene heterostructures for multiband coherent perfect absorption, Opt. Express 28 (2020) 37577–37589.
[17] K.-J. Peng, C.-L. Wu, Y.-H. Lin, H.-Y. Wang, C.-H. Cheng, Y.-C. Chi, G.-R. Lin, Saturated evanescent-wave absorption of few-layer graphene-covered side-polished single-mode fiber for all-optical switching, Nanophotonics 7 (1) (2018) 207–215.
[18] R. Deng, Y. Zhang, X. Wang, X.i. Xie, Y. Song, J. Bu, C. Min, X. Yuan, In situ intracellular Raman spectroscopic detection with graphene-based thermoelectric optical tweezers, Sens. Actuators B 361 (2022) 131722.
[19] F. Song, J. Zhang, T. Du, N. Wang, Z. Wang, Z. Zhang, B. Liu, Q. Zhang, Three-dimensional-printed hierarchical reduced graphene oxide/ethylenediamine filter with super-high uranyl ions with recycling capacity and unique selectivity, Carbon 182 (2021) 1–10.
[20] I.I. Tarasenko, A.F. Page, J.M. Hamm, O. Hess, Nonlocal quantum gain facilitates loss compensation and plasmon amplification in graphene hyperbolic metamaterials, Phys. Rev. B 99 (2019), 115430.
[21] W. Liang, L.I. Zheng, Y.U. Wang, W. Chen, Z.Y. Li, All-angle optical switch based on the zero reflection effect of graphene–dielectric hyperbolic metamaterials, Photonics Res. 7 (2019) 77–83.
[22] E. Sakr, P. Bermel, Angle-selective reflective filters for exclusion of background thermal emission, Phys. Rev. Appl. 7 (2017), 044020.
[23] N.W. Pech-May, M. Retsch, Tunable daytime passive radiative cooling based on a broadband angle selective low-pass filter, Nanoscale Adv. 2 (1) (2020) 249–255.
[24] L. Grineviciutea, C. Babayigitb, D. Gailevičiusc, E. Borb, M. Turdueve, V. Purlysc, T. Tolenisa, H. Kurtb, K. Staliunas, Angular filtering by Bragg photonic microstructures fabricated by physical vapour deposition, Appl. Surf. Sci. 481 (2019) 353–359.
[25] K. Ding, Z.Q. Zhang, C.T. Chan, Coalescence of spectral singularities and phase diagrams for one-dimensional PT symmetric photonic crystals, Phys. Rev. B 92 (2015) 1502.
[26] I.R. Howell, C. Li, N.S. Colella, K. Ito, J.J. Watkins, Strain-tunable one dimensional photonic crystals based on zirconium dioxide/slide-ring elastomer nanocomposites for mechanochromic sensing, ACS Appl. Mater. Interfaces 7 (6) (2015) 3641–3646.
[27] J. Lu, L. He, Z. Addison, E.J. Mele, B. Zhen, Floquet topological phases in one-dimensional nonlinear photonic crystals, Phys. Rev. Lett. 126 (2021), 113901.
[28] S. Park, V. Stinson, G. Boreman, T. Hofmann, Terahertz anisotropic response of additively manufactured one-dimensional photonic crystals, Optics Lett. 46 (2021) 3396–3399.
[29] H. Nemec, P. Kuzel, L. Duvillaret, A. Pashkin, M. Dressel, M.T. Sebastian, Highly tunable photonic crystal filter for the terahertz range, Opt. Lett. 30 (2005) 549–551.
[30] K.Y. Xu, X.C. Zheng, L. Li, W.L. She, Design of omnidirectional and multiple channeled filters using one-dimensional photonic crystals containing a defect layer with a negative refractive index, Phys. Rev. E 71 (2005), 066604.
[31] A. Alu, G.D. Aguanno, N. Mattiucci, M.J. Bloemer, Plasmonic Brewster angle: Broadband extraordinary transmission through optical gratings, Phys. Rev. Lett. 106 (2011), 123902.
[32] Y. Shen, D. Ye, L.i. Wang, I. Celanovic, L. Ran, J.D. Joannopoulos, M. Soljačić, Metamaterial broadband angular selectivity, Phys. Rev. B 90 (12) (2014), 125422.
[33] K.-T. Lee, C. Ji, D. Banerjee, L.J. Guo, Angular- and polarizationindependent structural colors based on 1D photonic crystals, Laser Photon. Rev. 9 (3) (2015) 354–362.
[34] A.P. Raman, M.A. Anoma, L. Zhu, E. Rephaeli, S. Fan, Passive radiative cooling below ambient air temperature under direct sunlight, Nature 515 (7528) (2014) 540–544.
[35] Y. Shen, D. Ye, I. Celanovic, S.G. Johnson, J.D. Joannopoulos, M. Soljačić, Optical broadband angular selectivity, Science 343 (6178) (2014) 1499–1501.
[36] H. Iizuka, N. Ngheta, E. Sugiura, Extremely small wavevector regime in a one-dimensional photonic crystal heterostructure for angular transmission filtering, Opt. Lett. 41 (2016) 3829–3832.
[37] H. Tanaka, I. Takai, H. Fujikawa, H. Iizuka, Nearly polarization-independent angular filters consisting of one-dimensional photonic crystals realized in the visible region, J. Lightwave Technol. 36 (12) (2018) 2517–2523.
[38] Y. Qu, Y. Shen, K. Yin, Y. Yang, Q. Li, M. Qiu, M. Soljačić, Polarization-independent optical broadband angular selectivity, ACS Photon. 5 (10) (2018) 4125–4131.
[39] B.F. Wan, H.F. Zhang, P.X. Wang, Nonreciprocal absorber with a narrow band of angular polarization sensitive regions based on a quasi-periodic structure, Opt. Lett. 46 (2021) 1934–1937.
[40] R. Ning, S. Liu, H. Zhang, B. Bian, X.A. Kong, Wide-angle broadband absorber in graphene-based hyperbolic metamaterials, Eur. Phys. J.-Appl. Phys. 68 (2014) 20401.
[41] S.N. Yin, Z.B. Zhu, X.F. Gao, Q. Wang, J. Yuan, Y. Liu, L.Y. Jiang, Terahertz nonreciprocal and functionality-switchable devices based on dielectric multilayers integrated with graphene and VO2, Opt. Lett. 47 (2022) 678–681.
[42] L.L. Ma, C.Y. Li, L.Y. Sun, Z.P. Song, Y.Q. Lu, B.X. Li, Submicrosecond electro-optical switching of one-dimensional soft photonic crystals, Photonics Res. 10 (2022) 786–792.
[43] F.Y. Lu, L. Gong, Y. Kuai, X. Tang, Y.F. Xiang, P. Wang, D.G. Zhang, Controllable optofluidic assembly of biological cells using an all-dielectric one-dimensional photonic crystal, Photonics Res. 10 (2022) 14–20.
[44] X.L. Zeng, W.B. He, M.H. Frosz, A. Geilen, P. Roth, G.K.L. Wong, P. St, J. Russell, B. Stiller, Stimulated Brillouin scattering in chiral photonic crystal fiber, Photonics Res. 10 (2022) 711–718.
[45] L. Zhou, Y. Zhou, Y.F. Zhu, X.X. Dong, L. Be, Y.Z. Gao, S.S. Wang, Broadband bidirectional visible light absorber with wide angular tolerance, J. Mater. Chem. C 4 (2016) 391.
[46] E. Sakr, P. Berme, Angle-Selective Reflective Filters for Exclusion of Background Thermal Emission, Phys. Rev. Appl 7 (2017), 044020.
[47] W. Xu, X. Hu, S. Zhuang, Y. Wang, X. Li, L. Zhou, S. Zhu, J. Zhu, Flexible and salt resistant janus absorbers by electrospinning for stable and efficient solar desalination, Adv. Energy Mater. 1702884 (2018).
[48] W. Ali, M.F. Mideksa, K. Hou, H. Li, X. Wang, Z. Tang, All-solution-processed ultrahigh broadband and wide-angle perfect absorber based on mxene-gold nanoparticles, Adv. Opt. Mater. 2000447 (2020).
[49] R. Chaurasiya, G.K. Gupta, A. Dixit, Heterostructure AZO/WSeTe/W(S/Se)2 as an efficient single junction solar cell with ultrathin janus WSeTe buffer layer, J. Phys. Chem. C 125 (2021) 4355–4362.
[50] M.S. Prasad, P.U. Bhaskar, S.R. Atchuta, P. Misra, B. Sobha, S. Sakthivel, Development of high-performance tandem layered absorber with wide-angular absorptance for solar thermal systems, Renew. Energy 176 (2021) 579e589.
[51] F. Wu, G. Lu, Z. Guo, H. Jiang, C. Xue, M. Zheng, C. Chen, G. Du, H. Chen, Redshift gaps in one-dimensional photonic crystals containing hyperbolic metamaterials, Phys. Rev. Appl 10 (2018), 064022.
[52] J. Wu, F. Wu, C. Xue, Z. Guo, H. Chen, Wide-angle ultrasensitive biosensors based on edge states in heterostructures containing hyperbolic metamaterials, Opt. Express 27 (2019) 24835.
[53] F. Wu, S. Xiao, Wide-angle high-efficiency absorption of graphene empowered by an angle-insensitive Tamm plasmon polariton, Opt. Express 31 (2023) 5722.